Proceedings World Geothermal Congress 2020+1
Reykjavik, Iceland, April - October 2021

# An Early Numerical Prediction of the United Downs Deep Geothermal Power Project, United Kingdom

Musa D. Aliyu, Rosalind A. Archer

Department of Engineering Science, the University of Auckland, Private Bag 92019, Auckland 1142, New Zealand

musa.aliyu@auckland.ac.nz

**Keywords:** Enhanced geothermal system, thermo-hydro-mechanical, United Downs Deep Geothermal Power Project, United Kingdom, COMSOL Multiphysics.

## ABSTRACT

The United Kingdom has been at the forefront of testing the feasibility of hot dry rock (HDR) geothermal energy resources since the mid-1970s. Several experiments were carried out between 1977 to 1991 at the Rosemanowes site in Cornwall. After a long period of testing the project was discontinued in 1991 due to some challenges. However, investors are back on board, developing a deep enhanced geothermal system (EGS) at the United Downs in Cornwall, Southwest England. The project aims to tap the abundant thermal energy underneath Cornish granites. So far, drilling of wellbores have been completed as of June 2019, and notable progress has been made on testing. Two features make the United Downs Deep Geothermal (UDDGP) project novel: a larger wellbore separation distance of about 2,882 m and the intersection of a fault zone by both wellbores. Thus, this paper presents a new three-dimensional (3D) model based on the site's limited data to predict system performance. The model implements the coupled effect of thermo-hydro-mechanical (THM) processes using the COMSOL Multiphysics. The simulation results show that the model prediction ability agrees with the existing EGS behaviour. However, more rigorous site data is required for an in-depth analysis of the system performance.

## 1. INTRODUCTION

The United Kingdom is getting back on board with developing an enhanced geothermal system (EGS) by drilling two deep boreholes at the United Downs in Cornwall, Southwest England. The project aims to tap the abundant thermal energy underneath Cornish granites for energy extraction. So far, drilling of wellbores have been completed as of June 2019, and notable progress has been made on testing (Geothermal Engineering Limited, 2020). The injection and production wellbores are drilled to depths of about 2,393 m and 5,275 m, respectively (Geothermal Engineering Limited, 2020). The vertical wellbore separation distance is approximately 2,882 m, making it first of its kind in EGS reservoirs. Both wellbores intersected a fault zone called Porthtowan Fault (PTF) with an uneven thickness of 200 m to 500 m (Ledingham et al., 2019). Connecting the wellbores via the fault structure is also a novel concept that has not been tested before.

The features above make many of the aspects of this project captivating and novel. Therefore, it presents a new chapter and challenge for geologists, scientists, and stakeholders in the geothermal community. The crucial challenges posed are understanding and predicting the behaviour of the system before and during exploitations. Understanding the system requires data availability such as the earth in situ stress, pore pressure and many other thermal, hydraulic, geomechanical and geochemical conditions. This information could help develop mathematical tools to mimic the complex multiphysics interactions during testing and exploitation stages.

The current project site is not far from the previous Rosemanowes hot dry rock (HDR) site experimented on earlier (Ledingham et al., 2019). The experience and knowledge obtained in the former project could shape and direct the current project's success. From this point of view, it is essential to present a brief history of the UK's attempts to explore HDR geothermal energy resources. The UK has been at the forefront in exploring deep geothermal energy resources as early as the mid-1970s (Richards et al., 1994). Several experiments were conducted between 1977–1991 at the Rosemanowes site in England to tap the Cornish granites' thermal energy (Macdonald et al., 1992). The experiments carried out resulted in Phase 1, Phase 2A, B and C, and Phase 3A. Phase 1 of the project involved testing tightly jointed granite at shallow depths (300 m) to assess the viability of connecting the wellbores by hydraulic stimulation (Macdonald et al., 1992). The results confirmed that it is feasible to enhance the permeability of the system and connect the wellbores (Parker and Jupe, 1995).

The success of Phase 1 led to the initiation of Phase 2 – intending to develop a reservoir at depths of about 2,000 m. The primary objective of Phase 2A (1980–1983) was to assess the possibility of creating a viable HDR subsurface heat exchanger. The proposed reservoir properties included creating a volume of 200 million $m^3$, comprising natural fractures with a fluid-rock contact area of 2 million $m^2$ (Batchelor, 1985). Several experiments were conducted, leading to Phases 2B and 2C (1983–1988) where further drilling of a new wellbore to a depth of about 2,600 m was carried out (Pine et al., 1987; Richards et al., 1994). However, at the end of Phase 2 experiments, several issues were encountered, including excessive temperature drawdown and water losses (Parker, 1999).

After Phase 2 ended with numerous unanswered questions, the project commissioned Phase 3 (1988–1991) for further stimulation and testing to improve the reservoir's performance (Atkins Ltd., 2013; Bruel, 1995). The experiment's outcome shows that a proper understanding of the earth stress regime and joint orientation could help create an optimal reservoir system (Abé et al., 1999). Based on the results obtained, the Camborne School of Mines (CSM) developed a modelling technique for evaluating the system's performance, resource sizing, and economic aspects (Parker and Jupe, 1995).

The three phases of the Rosemanowes project showed that significant capital expenditure is required to develop an EGS reservoir. The experience gained from Rosemanowes demonstrated the cost of having insufficient knowledge of the design factors and inadequate data beforehand (Parker and Jupe, 1995). Therefore, before a site is selected for development, it is necessary to conduct extensive feasibility studies. The availability of all the necessary data beforehand could minimise the cost of developing an optimal system. Mathematical modelling tools could help establish the conditions required to develop a suitable EGS reservoir and predict its performance. One modelling technique that can help us tackle these challenges is a reliable numerical model, because it can provide us with some crucial information for decision making in the various stages of the project.

This paper presents numerical modelling to design and predict the United Downs Deep Geothermal Power (UDDGP) system's performance. The goal is to illustrate how, when minimum site data is available, modelling tools can be effective in examining the feasibility of extracting thermal energy from the site. A three-dimensional (3D) numerical model of the UDDGP system is developed that implements the coupled effect of thermo-hydro-mechanical (THM) processes. The model is employed to analyse the fundamental reservoir parameters that affect the system behaviour under a long-term performance of 30 years. The parameters investigated include the production temperature, fault permeability, injection pressure, production flow rate, thermal energy extraction and impedance.

## 2. THE UDDGP PROJECT

This section presents brief information on the UDDGP Project conceptualisation. The information is extracted from two primary sources, the Geothermal Engineering Limited (GEL) website (Geothermal Engineering Limited, 2020) and a paper by Ledingham et al. (2019).

### 2.1 The UDDGP Concept

A study was carried out from the inception of the project on the best location to host a geothermal reservoir that would utilise the various fault zones present throughout Cornwall (Ledingham et al., 2019). It was agreed upon that the Porthtowan Fault (PTF) would be used, one of the northwest-southeast fault zones. The PTF zone extends from the north coast to the south coast, that is, from Porthtowan to Falmouth. It was observed in some of the mines that the PTF zone is of significant length with near-vertical linearity that is likely to persist to depth. The project was conceptualised on drilling two deep boreholes to intersect the PTF zone. The aim is to establish a circulation over a considerable vertical distance of the wellbores via the PTF zone (Ledingham et al., 2019). The larger well separation will allow enough mass flow rate and heat transfer for commercial energy extraction if the PTF zone's permeability is high enough.

Drilling of the production wellbore (i.e., UD-1) began on the 6$^{th}$ of November 2018 and ended on the 26$^{th}$ of April 2019. The wellbore was drilled to a depth of 5,275 m (i.e., measured depth MD) with a corresponding true vertical depth (TVD) of 5,057 m. The total number of bits used was 28, with different casing points and sizes (Geothermal Engineering Limited, 2020). From 0 to 11 m depth, 30–inch casing size was employed. Table 1 shows the casing sizes with the corresponding depths and hole sizes.

**Table 1: Production wellbore UD-1 casing and hole sizes**

| Depth (m) | Casing size (m) | Hole size (m) |
|---|---|---|
| 0 - 11 | 0.762 | - |
| 11 - 245 | 0.473 | 0.610 |
| 245 - 899 | 0.340 | 0.445 |
| 899 - 3985 | 0.245 | 0.316 |
| 3985 – 5275 | Open hole | 0.216 |

**Table 2: Injection wellbore UD-2 casing and hole sizes**

| Depth (m) | Casing size (m) | Hole size (m) |
|---|---|---|
| 0 - 11 | 0.762 | - |
| 11 - 804 | 0.340 | 0.445 |
| 804 - 1820 | 0.245 | 0.312 |
| 1820 – 2393 | Open hole | 0.216 |

On the 11$^{th}$ of May 2019, the injection wellbore drilling (i.e., UD-2) commenced and ended on the 28$^{th}$ of June 2019. The wellbore was drilled to a depth of 2,393 m (i.e., MD), which corresponds to a TVD of about 2,214 m. Different casing points and sizes were used in the wellbore with a total of 10 bits. Table 2 presents the casing and hole sizes with their corresponding depths. For both UD-1 and UD-2 directional drilling techniques were utilised for the wellbores to intersect the targeted PTF zone. For UD-1, the directional drilling kicked off from 3,400 m and ended at 5,275 m. Whereas for UD-2, it began from 1,030 m and ended at 2,393 m (Geothermal Engineering Limited, 2020).

Based on the details provided above, a schematic representation of the UDDGP project is shown in Figure 1. The diagram illustrates the different structures present on the system for virtualisation purposes, because it is challenging to capture all the structure with minimal data. Ledingham et al. (2019) reported that a granitic body was first intersected at about 210–230 m depth while drilling UD-1. A fine-grained microgranite dominated by kaolinite was encountered from 270 m to 700 m. At 750 m depth, a

coarser-grained, tourmaline-rich granite with a flaky texture was intersected. Chipping details on the site can be found on the GEL website (Geothermal Engineering Limited, 2020).

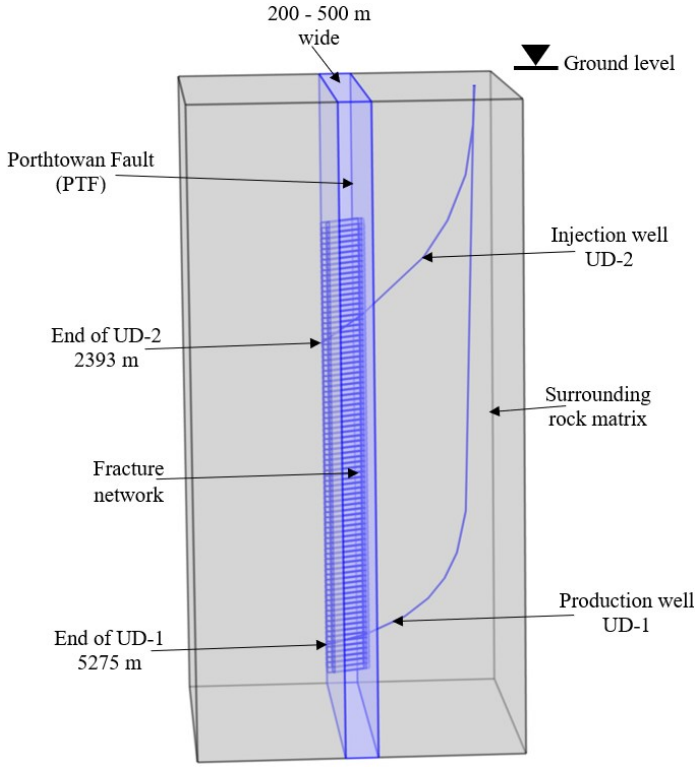


**Figure 1: Schematic diagram of UDDGP system.**

## 3. MATHEMATICAL DESCRIPTION OF THE UDDGP CONCEPT

This section deals with the mathematical description of the UDDGP Project. The system constitutes different structures including the rock mass, fault zone, fracture network and wellbores. Thus, the UDDGP project can be referred to as a multiple pore media system. Each of the media is represented by the governing set of equations, constitutive models and coupled functions to describe the system behaviour.

### 3.1 Model Assumptions

The mathematical model coupling thermal-hydraulic-geomechanical processes in porous media includes the conservation of mass, energy and momentum equations with Darcy's, Fourier's and Hooke's constitutive models. The assumptions of the model are as follows:

1. The rock matrix is homogeneous and isotropic.
2. The rock matrix is fully saturated with a single fluid.
3. The hydraulic process meets Darcy's law flow conditions.
4. The thermal process meets Fourier's law with local thermal balance.
5. The fluid properties change with the temperature.
6. The fault permeability changes with pore pressure and normal stress.

### 3.2 Fluid Flow Equations

Fluid flow in a fully saturated porous medium is defined by the continuity equation and Darcy's law, given as (Aliyu and Chen, 2017):

$$\frac{\partial}{\partial t}\left(\rho_L \phi\right) + \nabla \cdot \left(\rho_L v\right) = Q_m \tag{1}$$

where $\rho_L$ is the fluid density, $\phi$ is the solid porosity, $v$ is the Darcy's velocity field and $Q_m$ is the mass source term. The Darcy's velocity field is given as (Aliyu and Chen, 2018):

$$v = -\frac{\kappa}{\mu}\left(\nabla p + \rho_L g \nabla z\right) \tag{2}$$

where $\kappa$ is the permeability of the porous medium, $\mu$ is the fluid's dynamic viscosity, $g$ is acceleration due to gravity and $z$ is the vertical depth. Inserting (2) into (1) gives the generalised governing equation as:

$$\frac{\partial}{\partial t}(\rho_L \phi) + \nabla \cdot \rho_L \left( -\frac{\kappa}{\mu}(\nabla p + \rho_L g \nabla z) \right) = Q_m \tag{3}$$

In this study, the porous medium and the fluid are assumed compressible. Thus, the expression on the left-hand side of (3) is replaced with:

$$\frac{\partial}{\partial t}(\rho_L \phi) = \rho_L S \frac{\partial p}{\partial t} \tag{4}$$

By inserting the right-hand side of (4) into (3), the generalised governing equation takes the following form:

$$\rho_L S \frac{\partial p}{\partial t} + \nabla \cdot \rho_L \left( -\frac{\kappa}{\mu}(\nabla p + \rho_L g \nabla z) \right) = Q_m \tag{5}$$

where $S$ is the storage coefficient that defines the fluid's and porous medium's weighted compressibilities. If the storage is linearised, the subsequent model is employed to determine the storage, $S$ (Cheng, 2016):

$$S = \phi_e \chi_L + (1 - \phi)\chi_S \tag{6}$$

where $\phi_e$ is the effective porosity, $\chi_L$ is the fluid compressibility and $\chi_S$ is the effective solid compressibility.

### 3.3 Heat Transport Equations

The heat transport equation used in this study assumed a thermal balance between the solid and the fluid at any point in space and time. Thus, the generalised governing equation for the heat transfer in the porous medium is given as (Aliyu and Chen, 2017):

$$(\rho C_P)_e \frac{\partial T}{\partial t} + \rho_L C_{P,L} v \cdot \nabla T + \nabla \cdot q = Q \tag{7}$$

where $(\rho C_P)_e$ is the effective heat capacity, $T$ is the temperature, $q$ is the Fourier's conductive heat flux and $Q$ is the heat source/sink term. The effective heat capacity $(\rho C_P)_e$ is defined as (Aliyu and Chen, 2017):

$$(\rho C_P)_e = \phi \rho_S C_{P,S} + (1 - \phi)\rho_L C_{P,L} \tag{8}$$

where $\rho_S$ is the solid density, $C_{P,S}$ is the solid heat capacity and $C_{P,L}$ is the fluid heat capacity. The Fourier's conductive heat flux $q$ is defined as (Aliyu and Chen, 2016):

$$q = -\lambda_e \nabla T \tag{9}$$

where $\lambda_e$ is the effective thermal conductivity given as (Aliyu, 2018):

$$\lambda_e = \phi \lambda_S + (1 - \phi)\lambda_L \tag{10}$$

where $\lambda_S$ and $\lambda_L$ are the solid and the fluid thermal conductivities, respectively.

### 3.4 Geomechanical Process Equations

The force equilibrium equation is the fundamental equation for geomechanics, given as (Abé et al., 1976):

$$\nabla \cdot \sigma + F = 0 \tag{11}$$

where $\sigma$ is the total stress tensor and $F$ is the body or external force. Fluid flow in the porous medium can alter the medium's stresses and strains through fluid's pressure. The changes are represented by disintegrating the stress tensor into effective stress $\sigma'$ and pore pressure $p$, written as (Abé et al., 1985):

$$\sigma = \sigma' + \alpha p \tag{12}$$

where $\alpha$ is the Biot's coefficient. Substituting (12) into the force equilibrium equation (11), yields:

$$\nabla \cdot \sigma' + \alpha \nabla p + F = 0 \tag{13}$$

### 3.5 Fault Permeability Model

The equations presented above are the same for the rock matrix and the fault zone. However, the fault zone permeability changes with the variations of the pore pressure and overburden, confining stress. The function describing the fault zone's permeability is given as (Nathenson, 1999):

$$\kappa_F = \kappa_{F,0} \exp\left(\frac{c(p - p_0)}{\sigma_V}\right) \tag{14}$$

where $\kappa_{F,0}$ is the initial fault zone permeability, the exponent $c$ is a fitting parameter determined experimentally, $p_0$ is the initial pore pressure and $\sigma_V$ is the total overburden confining stress.

### 3.6 Mass Source and Sink

The mass source term is written as:

$$\int_{\partial S(r_w)} Q_m \partial S = M_0, with\ A_w = 2\pi r_w l_w, and\ r_w = \frac{d_w}{2} \tag{15}$$

where $A_w$ is the area of the wellbore, $r_w$ is the wellbore radius, $l_w$ is the length of the wellbore and $d_w$ is the diameter of the wellbore.

The mass sink term is given as:

$$\frac{1}{A_w} \int_{\partial S(r_w)} p \partial S = p_p \tag{16}$$

where $p_p$ is the specified production pressure.

### 3.7 Heat Source

The heat source term is written as:

$$\lim_{\partial S \to 0} \int_{\partial S} Q \partial S = Q_l \tag{17}$$

where $Q_l$ is the line heat source. The line heat source is defined as:

$$Q_l = C_{P,L} M_l (T_{inj} - T) \tag{18}$$

where $M_l$ is the mass flow rate per unit length and $T_{inj}$ is the injection temperature. The mass flow rate per unit length is given as:

$$M_l = M_0 l_w \tag{19}$$

### 3.8 Thermo-Hydro-Geomechanical Coupling

The fluid flow in the porous media can be affected by geomechanical deformations resulting from earth stress changes. Similarly, the porous media's stress regime can be impacted by fluid flow due to pore pressure changes. The coupled process that is triggered due to the fluid flow and geomechanical changes is called hydro-mechanical coupling. The poroelasticity theory describes the coupled system as (Cheng, 2016):

$$G\nabla^2 u + \left(K_d + \frac{G}{3}\right)\nabla \cdot (\nabla u) = \alpha \nabla p \tag{20}$$

$$\frac{1}{M}\frac{\partial p}{\partial t} - \nabla \cdot \left(\frac{\kappa}{\mu}(\nabla p - \rho_L g \nabla z)\right) = -\alpha \frac{\partial (\nabla \cdot u)}{\partial t} \tag{21}$$

where $G$ is the shear modulus, $u$ is the displacement, $K_d$ is the drained bulk modulus and $M$ is the Biot's modulus. The Biot's modulus is defined as (Cheng, 2016):

$$\frac{1}{M} = \frac{\alpha - \phi}{K_S} + \frac{\phi}{K_L} \tag{22}$$

where $K_S$ and $K_L$ are the solid and fluid bulk modulus, respectively.

The temperature changes on density, viscosity and thermal conductivity yielded the heat transport's coupled effect on fluid flow. For density changes with a temperature range from 20°C to 250°C, the fitting polynomial is given as (Aliyu and Chen, 2017):

$$\rho_L(T) = 996.9\left(1 - 3.17\times10^{-4}(T - 298.15) - 2.56\times10^{-6}(T - 298.15)^2\right) \tag{23}$$

The dynamic viscosity changes within a temperature range of 4°C to 250°C is expressed as (Aliyu and Chen, 2017):

$$\mu(T) = 2.414\times10^{-5}\times10^{\frac{247.8}{(T+133)}} \tag{24}$$

For the thermal conductivity in $10^3$ W/m/K, the fitting polynomial is given as (Aliyu and Chen, 2017):

$$\lambda_L(T) = -922.47 + 2839.5\left(\frac{T}{T_0}\right) - 1800.7\left(\frac{T}{T_0}\right)^2 + 525.77\left(\frac{T}{T_0}\right)^3 - 73.44\left(\frac{T}{T_0}\right)^4 \tag{25}$$

where $T_0$ is 273.15 K, and the temperature ranges between 0°C and 350°C.

The fluid flow's coupled effect on heat transport is achieved through Darcy's velocity field term provided in equation (7). The expression allows the convective heat transfer to contribute to the overall thermal process (Chen and Aliyu, 2017). The coupled effect of heat transport on the geomechanical process is accomplished via the thermal expansion coefficient (Aliyu et al., 2017). Likewise, the geomechanical process affects heat transfer through thermal capacity and strain energy.

### 3.9 Proposed Reservoir Geometry

The geometry of the proposed numerical model is shown in Figure 2. The system's actual geometry is reduced where the reservoir top begins from the open-hole section of UD-2. Therefore, the rock matrix dimension is 2,000 m × 2,000 m × 4,000 m and the PTF zone dimension is 300 m × 300 m × 4,000 m. For the wellbores, a diameter of about 216 mm is used, and only the open-hole (i.e., uncased) sections are presented. The inclined wellbores are curved due to directional drilling, and both intersected the PTF zone. The open-hole section of the UD-2 began from 1,820 m and ended at 2,393 m, whereas for UD-1, it started from 3,985 m and ended at 5,275 m. Table 3 presents the reservoir properties, and initial and boundary conditions are shown in Table 4.

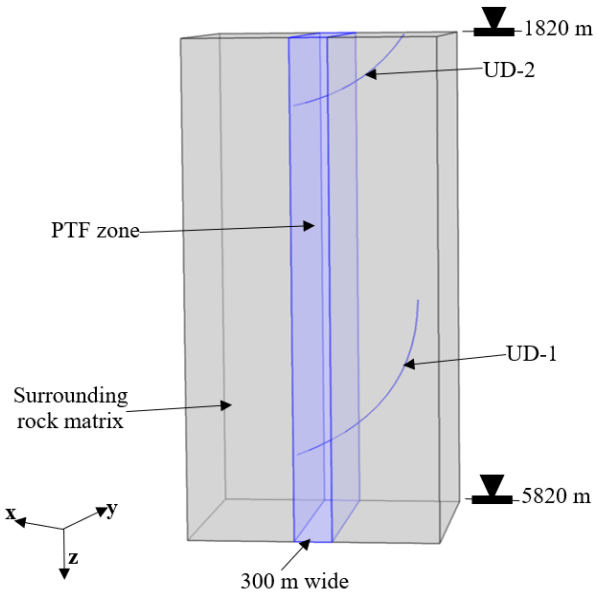


**Figure 2: Proposed reservoir geometry of UDDGP system.**

The equations and coupling functions presented in this section in conjunction with the properties and boundary conditions shown in Tables 3 and 4 are implemented in the COMSOL Multiphysics solver to obtain the simulation results. COMSOL Multiphysics is a platform to run the partial differential equations (PDEs) and the coupling functions using a finite element (FE) approach. The software has been validated against geothermal field experiments previously (Aliyu and Archer, 2021, 2020a, 2020b).

## 4. RESULTS AND ANALYSIS

This section analyses the simulation results based on the range of flow rates (i.e., 20 to 60 kg/s) proposed to be used at the UDDGP project. A parametric study is performed on how the system responds to the different flow rates. The crucial parameters analysed include the production temperature, production flow rate, fault permeability, thermal energy and impedance. Understandings the response of those parameters to different operational conditions could help us assess the long-term system performance.

### 4.1 The Effect of Flow Rate on Production Temperature

The production temperature curves for the different injection flow rates are shown in Figure 3. The flow rates employed are 20 kg/s, 30 kg/s, 40 kg/s, 50 kg/s and 60 kg/s. As can be seen, the higher the flow rate, the faster the drawdown in the production temperature. The convective heat transfer inside the fault system increased with the fluid flow increase, and fluid travelled longer within the fault than the surrounding rock matrix. The higher flow leads to early temperature breakthrough due to thermal front occurrence within the fault system. However, it enhances the fault permeability and reduces the chances of short-circuiting within the system.

**Table 3: Reservoir properties of the UDDGP system**

| Parameter | Symbol | Matrix Value | Fault Value | Unit |
|---|---|---|---|---|
| Thermal conductivity | $\lambda_S$ | 4.0 | 2.8 | W/m/K |
| Coefficient of thermal expansion | $\beta_S$ | 7e-6 | 7e-6 | 1/K |
| Heat capacity | $C_{P,S}$ | 920 | 900 | J/kg/K |
| Rock density | $\rho_S$ | 2500 | 2500 | kg/m$^3$ |
| Young's modulus | $E$ | 60 | 45 | GPa |
| Porosity | $\phi$ | 0.01 | 0.02 | - |
| Permeability | $\kappa$ | 1e-18 | Varies | m$^2$ |
| Vertical stress | $\sigma_V$ | 60 | 60 | MPa |
| Maximum horizontal stress | $\sigma_H$ | 52 | 52 | MPa |
| Minimum horizontal stress | $\sigma_h$ | 44 | 44 | MPa |
| Biot coefficient | $\alpha$ | 0.79 | 0.79 | - |
| Biot modulus | $M$ | 1.23e4 | 1.23e4 | MPa |
| Solid bulk modulus | $K_S$ | 50 | 50 | GPa |
| Exponent fitting parameter | $c$ | - | 15 | - |
| Initial fault permeability | $\kappa_{F,0}$ | - | 123 | mD |

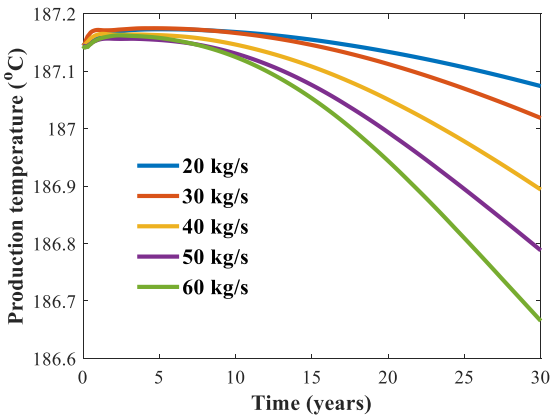


**Figure 3: Production temperature changes for the different injection flow rates.**

### 4.2 The Effect of Flow Rate on Injection Pressure

The pressure transient at the injection wellbore is shown in Figure; each of the five injection flow rates (i.e., 20 kg/s to 60 kg/s) has a similar pressure history. The higher the injection rate, the larger the pressure and vice versa. It is worth mentioning that, during the circulation, the fluid pressure increased to the minimum value required to sustain the injection rate; that is, the pressure needed to accommodate the injected fluid volume. Most of the injected fluid enters fault void space created due to permeability enhancement and fluid flow into the fault system.

### 4.3 The Effect of Flow Rate on Fault Zone Permeability

The fault permeability changes near the injection wellbore for the different injection flow rates are shown in Figure 5. At the end of the 30 years simulation, the permeability increased by about two orders of magnitude, from 1.22e-13 to 7.58e-11 for the highest flow rate (i.e., 60 kg/s), and 1.22e-13 to 2.22e-11 for the lowest flow rate (i.e., 20 kg/s). The corresponding pressure increase for the 60 kg/s and 20 kg/s injection flow rates are about 38.4 MPa and 35.2 MPa, respectively. Overall, the changes in the fault permeability agreed well with the injection pressure changes shown in Figure 4 due to the permeability model's dependence on both pore pressure and overburden confining stress.

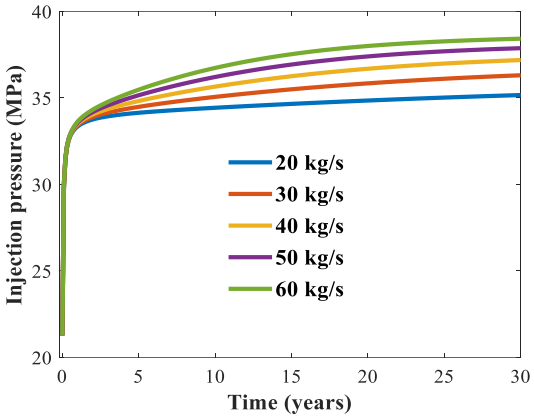


**Figure 4: Injection pressure changes for the different injection flow rates.**

**Table 4: The initial and boundary conditions employed for the UDDGP system**

| Physics | Boundary/Edge | Initial and boundary conditions |
|---|---|---|
| **Hydraulic** | Reservoir initial pressure | $p_0(t) = \rho_L \times g \times z(MPa),$ $0 \le t \le 30$ |
| | Injection wellbore (i.e., mass flow rate) | $M_0(t) = 20 - 60\ kg/s,$ $0 \le t \le 30$ |
| | Production wellbore (i.e., production pressure) | $p_p(t) = 10\,MPa,$ $0 \le t \le 30$ |
| | Surfaces (top, bottom, front, & back) except at the production areas. | $p(t) = 0,$ $0 \le t \le 30$ No flow |
| | Surfaces (left & right) | $p_0(t) = \rho_L \times g \times z(MPa),$ $0 \le t \le 30$ |
| **Geomechanics** | Reservoir initial stresses | $\sigma_{V_0}(t) = \sigma_V - \alpha \times p_0,$ $\sigma_{H_0}(t) = \sigma_H - \alpha \times p_0,$ $\sigma_{h_0}(t) = \sigma_h - \alpha \times p_0,$ $0 \le t \le 30$ |
| | Top surfaces | $\sigma_V(t) = 60\,MPa$ $0 \le t \le 30$ |
| | Front & back surfaces | $\sigma_H(t) = 52\,MPa,$ $0 \le t \le 30$ |
| | Left & right surfaces | $\sigma_h(t) = 44\,MPa,$ $0 \le t \le 30$ |
| | All surfaces except the top | $u(t) = 0,$ $0 \le t \le 0$ Roller boundaries |
| **Thermal** | Reservoir initial temperature | $T_i(t) = 12°C - (35°C/km) \times z(°C),$ $0 \le t \le 30$ |
| | Injection wellbore (i.e. injection temperature) | $T_{inj}(t) = 50°C$ $0 \le t \le 30$ |
| | Production wellbore (i.e. unknown temperature to be calculated) | $T_{pro}(t) = ?$ $0 \le t \le 30$ |
| | Surfaces (left & right) | $T_i(t) = 12°C - (35°C/km) \times z(°C),$ $0 \le t \le 30$ |
| | Surfaces (top, bottom, front & back) | $-n \cdot q(t) = 0,$ $0 \le t \le 30$ Thermally insulated |

### 4.4 The Effect of Production Pressure on Temperature

The effect of production pressures with low and high injection flow rates on the production temperature is shown in Figure 6. The extraction pressures employed are 5 MPa and 10 MPa with 20 kg/s and 60 kg/s injection flow rates. The results show that a low injection flow rate combined with a high production pressure yields a better extraction temperature. It is clear from the results that controlling the production pressure could help achieve optimal performance for the system.

### 4.5 Production Flow Rate

The changes over time of the production flow rates for different injection flow rates are shown in Figure 7. As can be seen, during the early stages of fluid circulation, lower flow rates are obtained at the production wellbore for the different scenarios due to insufficient fluid reaching the producer. The possible reason is that the producer's permeability remains intact in addition to the larger wellbore spacing. However, after five years, the fluid flow begins to build up in the reservoir by circulating down to the production wellbore. At the end of the 30 years simulation, the highest injection rate (i.e., 60 kg/s) reached a production flow rate of about 8 kg/s, equivalent to 13.4% of the injection flow rate. Whereas the lowest injection rate (i.e., 20 kg/s) attained a value of 2.53 kg/s, corresponding to 12.65% of the injection rate.

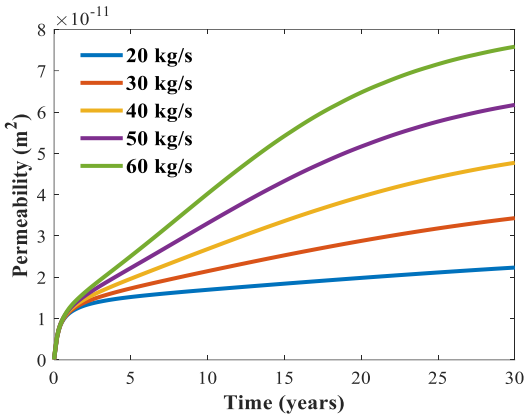


**Figure 5: Fault permeability changes at the injection wellbore location for the different injection flow rates.**

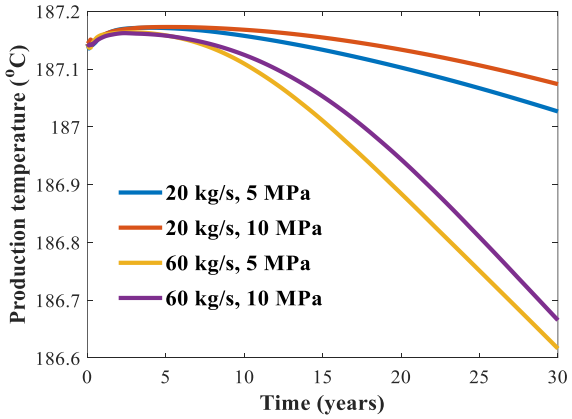


**Figure 6: Production temperature changes for high and low injection flow rates and pressures.**

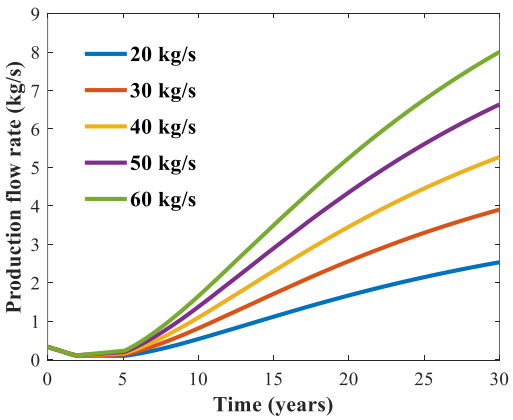


**Figure 7: Production flow rate changes for the different injection flow rates.**

### 4.6 The Effect of Flow Rate on Thermal Energy Extraction

The thermal energy at the production wellbore for the different injection flow rates is shown in Figure 8. The results show low thermal energy extraction during the first five years of the simulation for all the scenarios. Lack of adequate flow rate at the producer yielded the low output. After five years of simulation, the thermal energy continued to increase rapidly in all the injection cases. At the end of 30 years, the highest and the lowest injection flow rates (i.e., 60 kg/s and 20 kg/s) yielded about 4.6 MW and 1.4 MW of thermal energies, respectively. It shows that as the injection flow rate increases, the system's heat extraction rate increases significantly.

### 4.7 The Effect of Flow Rate on Impedance

The system impedance for the different injection flow rates is presented in Figure 9. The results show a drop in system impedance with the increase in the injection flow rate. For a maximum injection flow rate of 60 kg/s, the impedance ranges from 0.19 MPa/(kg/s) to 0.47 MPa/(kg/s) during the 30 years simulation. Whereas for a minimum injection flow rate of 20 kg/s, it ranges from 0.56 MPa/(kg/s) to 1.26 MPa/(kg/s). The result shows that the attainment of optimal reservoir performance for this system with low impedance is most likely to be achieved through high injection flow rate. Therefore, it is pertinent to examine the extent to which the injection flow rate will trigger fault slip and seismic events in the system.

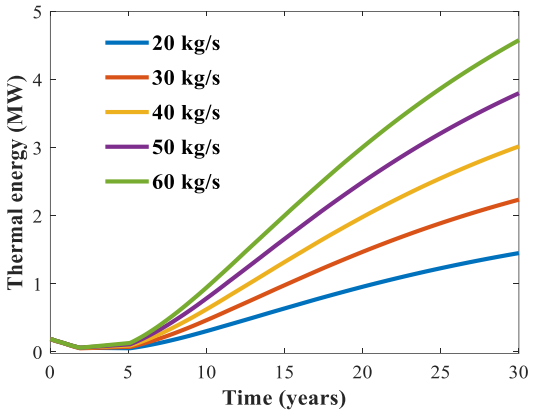


**Figure 8: Thermal energy curves at the production wellbore for the different injection flow rates.**

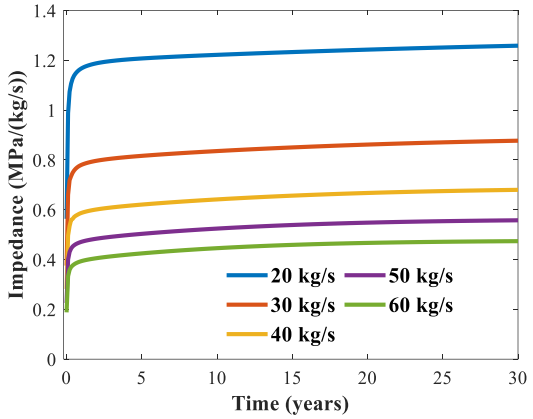


**Figure 9: Reservoir impedance changes for the different injection flow rates.**

## 5. CONCLUSION

A 3D numerical model of an enhanced geothermal system replicating the UDDGP system is presented. A finite element solver is employed to solve the thermo-hydro-geomechanical coupled response of the system. The proposed model is applied to examine the effects of different flow rates (i.e., 20 - 60 kg/s) on the system performance. The simulation results show that reservoir parameters are affected by the changes in the flow rates.

On the one hand, as expected, the system impedance reduces with the increase in the flow rate; that is, the higher the flow rate, the lower the impedance and vice versa. A similar response is seen with production temperature. On the other hand, the fault zone permeability increases with the increase in the flow rate: that is, the higher the flow rate, the larger the permeability. Similar behaviour is observed with injection pressure, thermal energy and production flow rate.

It is crucial to point out some issues concerning the proposed flow rates intended to be employed at the UDDGP project. The most pressing issue is that the flow rates are insufficient to connect the wellbores as indicated by the production flow rate. The highest production flow rate achieved was for the 60 kg/s injection scenario where just 8 kg/s was recovered. It requires an injection flow rate greater than 100 kg/s to accomplish a higher flow rate at the producer. Another concern is the propensity of the fault zone to slip due to a higher injection flow rate.

The modelling concept developed in this study is based on limited data sets available on the site. Thus, it is worth noting that the results should be treated with caution, because the model is in no way an actual representation of the site condition. Data availability, such as geological and geomechanical site conditions, could help develop a more rigorous model.

**REFERENCES**


Abé, H., Duchane, D. V., Parker, R.H., Kuriyagawa, M., 1999. Present status and remaining problems of HDR/HWR system design. Geothermics 28, 573–590.

Abé, H., Hayashi, K., Arima, S., 1985. Theoretical study on the stability of a reservoir created by the intersection of a fluid-filled crack with an oblique joint for the extraction of geothermal heat. Int. J. Numer. Anal. Methods Geomech. 9, 15–27.

Abé, H., Keer, L.M., Mura, T., 1976. Growth rate of a penny-shaped crack in hydraulic fracturing of rocks, 2. J. Geophys. Res. 81, 6292–6298.

Aliyu, M.D., 2018. Hot dry rock reservoir modelling. University of Greenwich.

Aliyu, M.D., Archer, R.A., 2020a. Numerical simulation of HDR geothermal energy reservoirs: A thermo-hydro-mechanical model. Geotherm. Resour. Counc. Trans. 44, 1145–1169.

Aliyu, M.D., Archer, R.A., 2020b. Thermo-hydro-mechanical model of multifracture HDR geothermal reservoirs. Geotherm. Resour. Counc. Trans. 44, 403–428.

Aliyu, M.D., Archer, R.A., 2021. Numerical simulation of multifracture HDR geothermal reservoirs. Renew. Energy 164, 541–555.

Aliyu, Musa D., Chen, H.-P., 2017. Sensitivity analysis of deep geothermal reservoir: Effect of reservoir parameters on production temperature. Energy 129, 101–113.

Aliyu, M.D., Chen, H.-P., 2018. Enhanced geothermal system modelling with multiple pore media: Thermo-hydraulic coupled processes. Energy 165, 931–948.

Aliyu, M.D., Chen, H., 2016. Numerical modelling of coupled hydro-thermal processes of the Soultz heterogeneous geothermal system. In: Proceedings of the VII European Congress on Computational Methods in Applied Sciences and Engineering (ECCOMAS Congress 2016). Institute of Structural Analysis and Antiseismic Research School of Civil Engineering National Technical University of Athens (NTUA) Greece, Athens, pp. 1659–1671.

Aliyu, Musa D, Chen, H., 2017. Optimum control parameters and long-term productivity of geothermal reservoirs using coupled thermo-hydraulic process modelling. Renew. Energy 112, 151–165.

Aliyu, M.D., Chen, H., Harireche, O., Hills, C.D., 2017. Numerical Modelling of Geothermal Reservoirs with Multiple Pore Media. In: PROCEEDINGS, 42nd Workshop on Geothermal Reservoir Engineering Stanford University, Stanford, California, February 13-15, 2017 SGP-TR-212. Stanford, US, pp. 1–12.

Atkins Ltd., 2013. Deep Geothermal Review Study. Final Report 156.

Batchelor, A.S., 1985. Progress in hot dry rock exploitation. Int. J. Energy Res. 9, 377–390.

Bruel, D., 1995. Heat extraction modelling from forced fluid flow through stimulated fractured rock masses: application to the Rosemanowes hot dry rock reservoir. Geothermics 24, 361–374.

Chen, H., Aliyu, M.D., 2017. Numerical Modelling of Coupled Thermo-Hydraulic Problems for Long-Term Geothermal Reservoir. In: VII International Conference on Computational Methods for Coupled Problems in Science and Engineering COUPLED PROBLEMS 2017 M. Papadrakakis, E. Oñate and B. Schrefler (Eds) NUMERICAL. pp. 234–243.

Cheng, A.H.-D., 2016. Poroelasticity, Theory and Applications of Transport in Porous Media Alexander, Theory and Applications of Transport in Porous Media. Springer International Publishing, Cham.

Geothermal Engineering Limited, 2020. United Downs Deep Geothermal Power Poroject [WWW Document]. Website. URL https://geothermalengineering.co.uk/united-downs/ (accessed 1.16.21).

Ledingham, P., Cotton, L., Law, R., 2019. The United Downs Deep Geothermal Power Project. Proc. 44th Work. Geotherm. Reserv. Eng. 1–11.

Macdonald, P., Stedman, A., Symons, G., Ora, O.O.X., 1992. The UK Geothermal Hot Dry Rock R & D Programme. 17th Work. Geotherm. Reserv. Eng. 5–11.

Nathenson, M., 1999. The dependence of permeability on effective stress from flow tests at hot dry rock reservoirs at Rosemanowes (Cornwall) and Fenton Hill (New Mexico). Geothermics 28, 315–340.

Parker, R., 1999. The Rosemanowes HDR project 1983-1991. Geothermics 28, 603–615.

Parker, R.H., Jupe, A.J., 1995. The role of reservoir modelling in feasibility studies for HDR geothermal energy exploitation. Geothermics 24, 301–305.

Pine, R., Baria, R., Pearson, R., Kwakwa, K., McCartney, R., 1987. A technical summary of phase 2b of the camborne school of mines HDR project, 1983–1986. Geothermics 16, 341–353.

Richards, H.G., Parker, R.H., Green, A.S.P., Jones, R.H., Nicholls, J.D.M., Nicol, D.A.C., Randall, M.M., Richards, S., Stewart, R.C., Willis-Richards, J., 1994. The performance and characteristics of the experimental hot dry rock geothermal reservoir at Rosemanowes, Cornwall (1985–1988). Geothermics 23, 73–109.